
RANDOMIZED SPECTRAL SAMPLING FOR EFFICIENT SIMULATION OF LASER PROPAGATION THROUGH OPTICAL TURBULENCE

A PREPRINT

Daniel A. Paulson *

Department of Electrical and Computer Engineering
University of Maryland
College Park, MD 20742, USA
dpaulson@umd.edu

Chensheng Wu

Department of Electrical and Computer Engineering
University of Maryland
College Park, MD 20742, USA

Christopher C. Davis

Department of Electrical and Computer Engineering
University of Maryland
College Park, MD 20742, USA

May 17, 2022

ABSTRACT

We present a new method for the generation of atmospheric turbulence phase screens based on the frequency shift property of the Fourier transform. This method produces low spatial frequency distortions without additional computation time penalties associated with methods using subharmonic subgrids. It is demonstrated that for simulations of atmospheric turbulence with finite outer scales, the performance of our method with respect to the statistical phase structure of the screen meets or exceeds other methods with respect to agreement with theory. We outline small-scale accuracy issues associated with modelling non-Kolmogorov spectral power laws using existing techniques, and propose a solution. For simulations of long-range propagation through atmospheric optical turbulence, our method provides various advantages over standard methods.

Keywords Optical Propagation · Atmospheric Turbulence · Optical simulations · Beam propagation method · Wave propagation · Optical turbulence · Atmospheric propagation · Computer simulations

1 Introduction

The split-step propagation method for modeling optical propagation through atmospheric turbulence has been widely used in statistical analysis of beam propagation since its introduction by Fleck, et al. [1, 2]. This method remains popular in simulations of long-range, linear optical propagation due to computation time advantages associated with using the Fast Fourier Transform (FFT) algorithm to compute the Discrete Fourier Transform (DFT), which are used in both the optical propagation and atmospheric distortion algorithms of the cited method. In simulations of nonlinear optical propagation phase screens are also widely used [3, 4, 5, 6], including when supporting studies centering on filamentation [7, 8, 9, 10, 11, 12]. However, due to circular shift symmetry and aliasing affects associated with the DFT, significant effort has gone into the development of computational methods which add subharmonic, low-spatial-frequency components to the atmospheric screens [13, 14]. Additionally, Zernike-polynomial-based methods [15] and other creative methods [16, 17] have been pioneered partly to address this issue. However, due to the computational efficiency of leveraging the FFT algorithm, DFT-based methods for phase screen generation remain popular [18, 19, 20, 21, 22, 23].

*Corresponding author.

We present a modified method which exploits the Fourier transform shift theorem [24], which also extends to the DFT [25], in order to include low frequency components in an FFT-centric method in a straightforward manor. For many applications, this method may provide sufficient phase screen accuracy relative to theory without additional computational penalty associated with subharmonics and other methods. Additionally the method can be combined with the subharmonic method of Lane, et. al [13] in order to give very accurate results across a range of spectral models of practical and theoretical importance. Section 2 discusses the basic method and results of use for bounded spectral models where it is well suited. Section 3 discusses the use of the method in concert with subharmonics, as well as other improvements. Finally, Section 4 summarizes results and discusses possible applications.

2 Randomized FFT-based Sampling

2.1 Algorithm

Central to the study of optical turbulence is the index of refraction structure function, $D_n(\vec{r})$, defined as [26]:

$$D_n(\vec{r}) = \left\langle (f(\vec{r} + \vec{r}_o) - f(\vec{r}_o))^2 \right\rangle \quad (1)$$

As for any real function, structure is related to the field's three dimensional energy spectrum, $\Phi_n(\vec{\kappa})$, by the following relationship [26]:

$$D_n(\vec{r}) = 2 \int_{-\infty}^{\infty} \Phi_n(\vec{\kappa}) [1 - \cos(\vec{r} \cdot \vec{\kappa})] d^3\vec{\kappa} \quad (2)$$

Traditional phase screen simulations using square grids [1, 2, 13, 14, 19] approximate the continuous energy spectrum as discrete, and generate complex screens as per:

$$\begin{aligned} \theta(j, l) &= \sum_{n, m=0}^{M-1} \tilde{c}(n\Delta\kappa_x, m\Delta\kappa_y) \exp[2\pi i(jn + lm)/M] \\ &= \sum_{n, m=0}^{M-1} \tilde{c}(n\Delta\kappa_x, m\Delta\kappa_y) \exp[i(j\Delta x \Delta\kappa_x + l\Delta y \Delta\kappa_y)] \end{aligned} \quad (3)$$

where $i = \sqrt{-1}$, Δx and Δy are the grid spacings in the x - and y -directions, M the number of grid points along each axis, and $\Delta\kappa_x$ and $\Delta\kappa_y$ are the spatial wavenumber grid spacings in the x - and y -directions. We note the relation, $\Delta x \Delta\kappa_x = \Delta y \Delta\kappa_y = 2\pi/M$. $\tilde{c}(n\Delta\kappa_x, m\Delta\kappa_y)$ is a random function defined by:

$$\tilde{c}(\beta, \gamma) = \Delta\kappa_x \Delta\kappa_y \cdot k \cdot (a + ib) \sqrt{2\pi \Delta z \Phi_n(\beta \hat{e}_x + \gamma \hat{e}_y)} \quad (4)$$

where β and γ are *dummy*-variables, $k = 2\pi/\lambda$ is the optical wavenumber (with λ the wavelength in vacuum), a and b are Gaussian random variables with variances of one, and \hat{e}_x and \hat{e}_y are unit vectors in the x - and y -directions. It is also important to note that for use with discretized simulations, the use of the function Φ_n in Eq. 4 must consider aliasing of spatial angular frequencies greater than $\pi/(M\Delta x)$ to negative frequencies (see supplemental material).

Eq. 3 represents a Fourier series using elements which are all harmonic across the spatial basis, creating a periodic boundary condition [1]. Investigating the effect the $\tilde{c}(0, 0)$ term has on the summation in Eq. 3, we note that it results in only the addition of a constant phase term across all of $\theta(j\Delta x, l\Delta y)$. This constant phase rotation term does not contribute tip, tilt, focus or defocus effects at any scale, or otherwise contribute to the behavior of the propagating field. Should $\Phi_n(0, 0)$ have a large enough value quantization error [25] will result. $\tilde{c}(0, 0)$ is commonly set to zero in practice [14, 19], which avoids these issues.

In defining a new type of complex phase screen, θ_R , we propose a more meaningful use of the point closest to the κ -space origin by virtue of:

$$\begin{aligned} \theta_R(j, l) &= \sum_{n, m=0}^{M-1} \tilde{c}(n\Delta\kappa_x + \delta\kappa_x, m\Delta\kappa_y + \delta\kappa_y) \\ &\quad \cdot \exp[i(j\Delta x(n\Delta\kappa_x + \delta\kappa_x) + l\Delta y(m\Delta\kappa_y + \delta\kappa_y))] \end{aligned} \quad (5)$$

where $\delta\kappa_x$ and $\delta\kappa_y$ are random variables described by a uniform distribution bound by $\pm\Delta\kappa_x/2$ and $\pm\Delta\kappa_y/2$, respectively. This offsets the lowest wavenumber grid point away from the origin, along with also translating the rest of

the sampling grid in the frequency domain. By allowing $\tilde{c}(n\Delta\kappa_x + \delta\kappa_x, m\Delta\kappa_y + \delta\kappa_y)$ to define the elements of a matrix, $\tilde{C}(n, m)$, we find that Eq. 5 is implementable via inverse FFT as per:

$$C(j, l) = M^2 \cdot \mathcal{F}_2^{-1}[\tilde{C}(n, m)] \quad (6)$$

$$\theta_R(j, l) = \exp[i(j\Delta x \delta\kappa_x + l\Delta y \delta\kappa_y)] \cdot C(j, l) \quad (7)$$

where $\mathcal{F}_2^{-1}[\cdot]$ in Eq. 6 denotes the two dimensional inverse FFT operator. Alternatively, the FFT can be used directly with appropriate conditioning of the C matrix (see supplemental material).

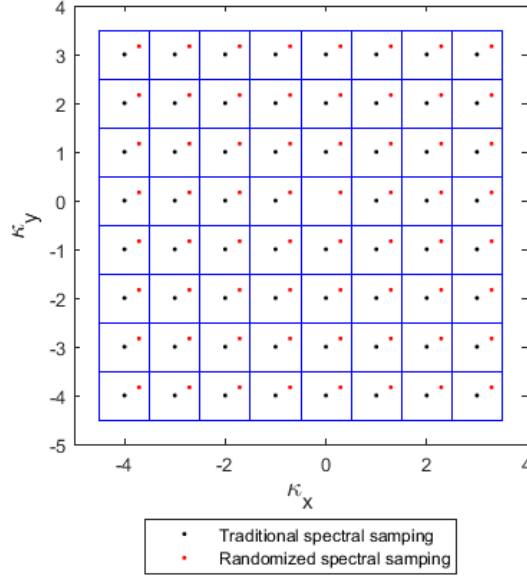


Figure 1: Visual aid showing traditional spectral sampling approach versus randomized spectral sampling approach in κ -space. Black dots represent traditional sampling points, red dots represent one realization of the randomized sampling approach, and the blue grid lines demarcate the sampling boundaries for the randomized method.

Fig. 1 juxtaposes the sampling methods discussed, and considers the affect of aliasing spatial frequency components in the second Nyquist zone to negative frequencies. The convention of setting $\tilde{c}(0, 0)$ to zero is reflected by the lack of a traditional spectral sampling grid point at the origin. $\theta_R(j, l)$ represents a single complex-number valued phase screen, with the real and imaginary parts therein defining a pair of real-number valued phase screens. Simulated atmospheric turbulence distortion is applied via multiplication of our complex propagating beam or wave by $\exp(i \cdot \text{Re}[\theta_R(j, l)])$ or $\exp(i \cdot \text{Im}[\theta_R(j, l)])$, where Re and Im functions represent taking the real and imaginary parts of an array, respectively.

$\theta_R(j, l)$ and the real valued phase screens it produces no longer exhibit a periodic boundary condition, and will have basis-wide low spatial frequency distortions. Additionally, we find the difference in computation time between the algorithm given in Eq. 3 and Eq. 5 to be negligible. The phase screens shown in Fig. 2 and Fig. 3 were generated using the popular approximation to the Hill Spectrum [27] developed by Andrews [28, 29], known commonly as the modified atmospheric spectrum. This spectral model is discussed in detail in subsequent sections. Note that tip and tilt components can be seen across the $x = 0$ and $y = 0$ axes, respectively, in the screen show in Fig. 3. Additionally, Fig. 2 displays a periodic boundary condition [1], in that should one circularly shift [25] the phase screen in either or both directions no sharp discontinuities would be apparent within the boundaries of the screen.

2.2 Results for bounded spectral models

The most widely used three dimension spectral model of atmospheric turbulence is derived from A. Kolmogorov's famous $2/3$'s law as [26, 29]:

$$\Phi_n(\vec{\kappa}) = 0.033 \cdot C_n^2 \cdot |\vec{\kappa}|^{-11/3} \quad (8)$$

This model is popular due to it's simple formulation, and approximate accuracy when the beam statistics of interest are within the inertial subrange of turbulence. However, this spectrum diverges at the κ -space origin leading to unphysical

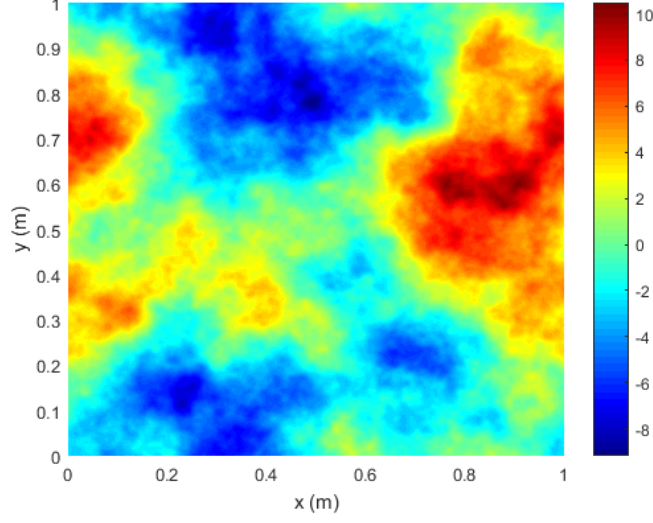


Figure 2: Phase screen produced using traditional FFT-based algorithm on 2048×2048 grid. The colors shown denote the phase shift of the screen in radians on the simulated propagating wave as per the colorbar.

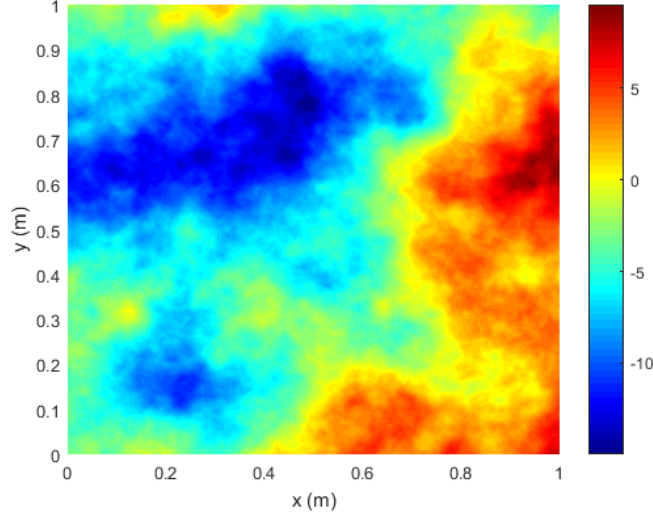


Figure 3: Phase screen produced using modified FFT-based algorithm on 2048×2048 grid displaying the lack of a periodic boundary condition. As in Fig. 2, the color of the screen denotes the phase shift.

properties such as containing infinite energy, divergent covariances, lack of a viscosity driven minimum feature size, and lack of a maximum feature size [29]. For these reasons, we will refer to this type of spectral model as *unbounded*. As we will demonstrate in the next section, additional modifications to the FFT-based algorithm may be required to accurately model unbounded spectral models using phase screens, as is the case for Kolmogorov turbulence.

We turn our attention to a practical atmospheric turbulence spectral model which accounts for inner scale, l_0 , and outer scale, L_0 , bounds on the inertial subrange, as well as intricacies of the experimentally observed energy spectra at higher spatial frequencies [30, 31, 27]. The modified atmospheric spectrum is given by Andrews [28, 29]:

$$\Phi_n(\vec{\kappa}) = 0.033 \cdot C_n^2 \cdot f_n\left(\frac{\kappa}{\kappa_l}\right) \cdot \frac{\exp(-\kappa^2/\kappa_l^2)}{(\kappa^2 + \kappa_0^2)^{11/6}} \quad (9)$$

where $\kappa_l = 3.3/l_0$, $\kappa_0 = 2\pi/L_0$, $\kappa = |\vec{\kappa}|$, and we define the function f_n as:

$$f_n(x) = 1 + 1.802x - 0.254x^{7/6} \quad (10)$$

As this spectral model does not present the same complications as that of Eq. 8, we refer to this as a *bounded* spectral model.

To assess the accuracy of the revised method, we must designate our metrics of interest. We had previously defined the refractive index three dimensional structure function, $D_n(\vec{r})$, via the spectral model of interest in Eq. 1. The structure function we are interested in, however, is that of an atmospheric phase screen which approximates the cumulative effects of optical propagation through a finite propagation distance, Δz . We denote this function as $D_\theta(\vec{r}_\perp)$, where $\vec{r}_\perp = x\hat{e}_x + y\hat{e}_y$. $D_\theta(\vec{r}_\perp)$ is defined by the two dimensional integral over all $\vec{\kappa}_\perp = \kappa_x\hat{e}_x + \kappa_y\hat{e}_y$ as per [14]:

$$D_\theta(\vec{r}_\perp) = 4\pi k^2 \Delta z \int_{-\infty}^{\infty} \Phi_n(\vec{\kappa}_\perp) [1 - \cos(\vec{r}_\perp \cdot \vec{\kappa}_\perp)] d^2\vec{\kappa}_\perp \quad (11)$$

For the modified atmospheric spectrum, though we are aware of closed-form approximations of turbulent structure functions for plane waves applicable to our analysis [32], we have instead developed our theoretical structure function via numerical integration of the equivalent form for isotropic turbulence:

$$D_\theta(\rho) = 8\pi^2 k^2 \Delta z \int_0^\infty \kappa_\rho \Phi_n(\kappa_\rho) [1 - J_0(\rho\kappa_\rho)] d\kappa_\rho \quad (12)$$

where $\rho = |\vec{r}_\perp|$, $\kappa_\rho = |\vec{\kappa}_\perp|$, and J_0 denotes the zeroth-order Bessel function of the first kind.

It is well documented that aliasing effects associated with the FFT-based propagation step of the split-step algorithm make parts of the simulation basis unusable [1, 19, 33, 34]. For this reason, a region of interest must be defined, which drives properties of the simulation. Number of grid points, simulated resolution, as well as the propagation distance between screens must be chosen carefully [19]. This requires consideration of many factors, including wavelength, coherence lengths, aperture sizes, etc. As a practical matter, many studies explicitly dedicate half of the x - and y -domain of simulation as guard bands to protect against edge effect aliasing [35, 36]. Additionally, the requirement of grid sizes greater than or equal to twice the size of the limiting apertures (or regions of interest) is explicit in some analysis of simulated propagation using changes of scale between the source and observation planes [33, 34]. In our own simulations of Gaussian beam propagation [20, 37, 38], we typically constrain the beam diameter to half the basis of simulation in each x - and y -direction in order to avoid edge aliasing effects. In order to present our results in a simple fashion, we assume that most users would have a region of interest defined by approximately this inner portion of the simulation basis.

Defining the measured x -direction structure along the $M/2^{th}$ row from the $M/4^{th}$ point to the $M/4 + j^{th}$ point as $D_x(j\Delta x)$, and y -direction structure along the $M/2^{th}$ column for its corresponding points as $D_y(l\Delta y)$, we can define our percent root mean square (RMS) error metric, \mathcal{E} , in terms of the D_θ defined by Eq. 12 via the equations:

$$\mathcal{E}_x = \sqrt{\frac{2}{M} \sum_{j=1}^{M/2} \left(\frac{D_x(j\Delta x) - D_\theta(j\Delta x)}{D_\theta(j\Delta x)} \right)^2} \quad (13)$$

$$\mathcal{E}_y = \sqrt{\frac{2}{M} \sum_{l=1}^{M/2} \left(\frac{D_y(l\Delta y) - D_\theta(l\Delta y)}{D_\theta(l\Delta y)} \right)^2} \quad (14)$$

$$\mathcal{E} = 100\% \times \frac{\mathcal{E}_x + \mathcal{E}_y}{2} \quad (15)$$

It should also be noted that as part of this study, the diagonal direction structure was also assessed, with similar results. However, because the grid diagonals are not orthogonal to the x - and y -directions those metrics are not included in our overall statistics.

We have found that for the range of outer scale values from one to one thousand times the basis of simulation, the RMS error as a percent assessed over half the simulation basis is constrained to less than 4%. More precisely, errors observed over the range $1 \leq L_0/(M\Delta x) \leq 10^3$ ranged from 0.34% - 3.79%. For the unrandomized grid, errors ranged from 2.57% - 61.51% over the same region. Fig. 4 displays the Monte-Carlo simulation results over 25,000 complex phase screens. All data in this study was collected using MATLAB. Because each complex screen contains a real and imaginary component, and structure is computed over orthogonal x - and y -directions, this simulation set contains 100,000 independent samples per point. Results are not shown for 512×512 or 1024×1024 traditional grids due to overlap of the plotted results, i.e. the results were largely indiscernible from the 2048×2048 traditional grid results.

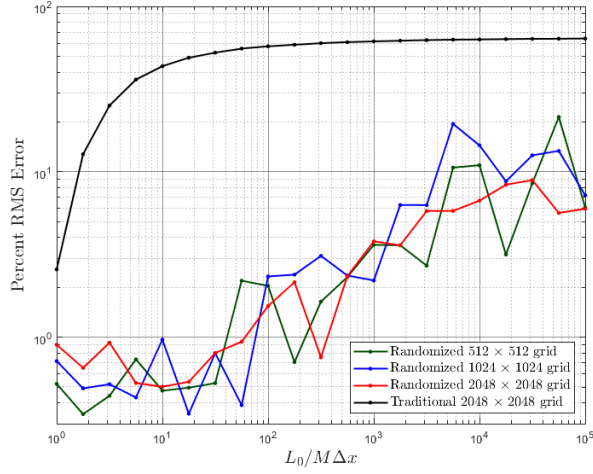


Figure 4: RMS error as a percent relative to theory over 50,000 phase screens trials for the simulated basis region of interest as parametrized by the outer scale, L_0 . 512×512 , 1024×1024 , 2048×2048 grid results are shown for randomized method. For the traditional method the 2048×2048 grid is shown.

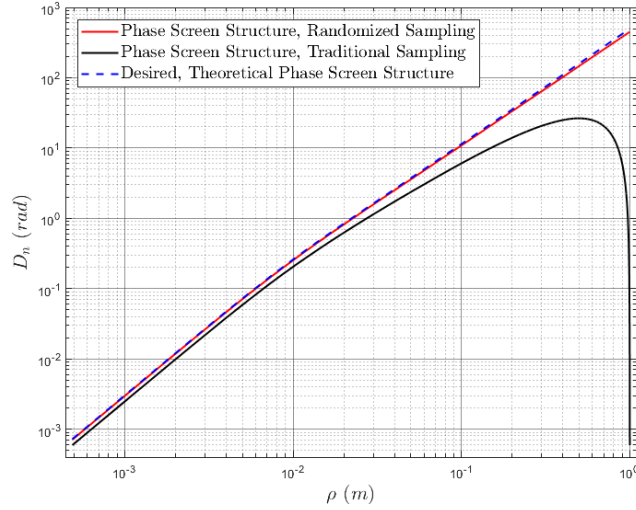


Figure 5: Comparison of phase screen structure versus theory using 2048×2048 grid, inner scale 1 cm, outer scale 100 km, $\Delta z = 500$ m, $\lambda = 1060$ nm, and $C_n^2 = 10^{-14} \text{ m}^{-2/3}$.

3 Hybrid method for use with bounded and unbounded spectral models

3.1 Core Algorithm

The modified algorithm discussed in the previous section was first investigated with regards to unbounded, anisotropic, non-Kolmogorov spectral models [38]. Therein it was discovered that for structure power laws greater than the $2/3$'s of Kolmogorov the randomized algorithm alone was not sufficient to ensure accurate statistics of observed simulated structure. For this reason, we have developed an algorithm utilizing both FFT-based frequency sampling randomization and subharmonic frequency sampling randomization. We define the following:

$$\theta_R(j, l) = \sum_{n,m=1}^{M-1} \tilde{c}(n\Delta\kappa_x + \delta\kappa_x, m\Delta\kappa_y + \delta\kappa_y) \cdot \exp[i(j\Delta x(n\Delta\kappa_x + \delta\kappa_x) + l\Delta y(m\Delta\kappa_y + \delta\kappa_y))] \quad (16)$$

$$\begin{aligned} \theta_{out}(j, l, p) = 3^{-2p} \sum_{n, m=-1}^1 (1 - \delta[n, m]) \\ \cdot \tilde{c} \left(\frac{n\Delta\kappa_x + \delta\kappa_x}{3^p}, \frac{m\Delta\kappa_y + \delta\kappa_y}{3^p} \right) \\ \cdot \exp \left[i \left(j\Delta x \frac{n\Delta\kappa_x + \delta\kappa_x}{3^p} \right. \right. \\ \left. \left. + l\Delta y \frac{m\Delta\kappa_y + \delta\kappa_y}{3^p} \right) \right] \end{aligned} \quad (17)$$

$$\begin{aligned} \theta_{in}(j, l) = 3^{-2(N_p+1)} \cdot \tilde{c} \left(\frac{n\Delta\kappa_x + \delta\kappa_x}{3^{N_p+1}}, \frac{m\Delta\kappa_y + \delta\kappa_y}{3^{N_p+1}} \right) \\ \cdot \exp \left[i \left(j\Delta x \frac{n\Delta\kappa_x + \delta\kappa_x}{3^{N_p+1}} \right. \right. \\ \left. \left. + l\Delta y \frac{m\Delta\kappa_y + \delta\kappa_y}{3^{N_p+1}} \right) \right] \end{aligned} \quad (18)$$

In Eq. 18 N_p is the number of subharmonic *constellations* of sampled frequencies (groups of 8 subharmonics chosen from common subgrid boundaries) and $\delta[n, m]$ is the two dimensional discrete Dirac delta function ($\delta[n, m] = 1$ for $n = m = 0$, otherwise $\delta[n, m] = 0$) which we use to ignore the central point of each constellation. It is very important to note that in Eqs. 17 and 18, we choose a different $\delta\kappa_x, \delta\kappa_y$ for each element of the summation (see Fig. 6). That is, for any index (n, m) change in in Eq. 17 or 18 we choose a new $\delta\kappa_x, \delta\kappa_y$ according to a uniform distribution.

The final *hybrid* phase screen, θ_H , is given by:

$$\theta_H(j, l) = \theta_R(j, l) + \theta_{in}(j, l) + \sum_{p=1}^{N_p} \theta_{out}(j, l, p) \quad (19)$$

The sampling approach described by Eq. 19 can be visualized by Fig. 6 for $N_p = 1$. We have found by choosing the correct number of subharmonic constellations, N_p , Eq. 19 yields very accurate results for any reasonable spectral model. We shall demonstrate results for both bounded and unbounded spectral later in this section.

3.2 Phase Screen Whitening for Subresolution Inner Scales

Since the introduction of generalized spectral models by Kon [39], much theoretical work has gone into the study of wave propagation through anisotropic, non-Kolmogorov turbulence defined by unbounded refractive index spectra [40, 41, 42, 43, 22, 44, 45]. These spectral models are derived from the structure function of refractive index of the form:

$$D_n(x, y, z) = \tilde{C}_n^2 \left(\frac{x^2}{\mu_x^2} + \frac{y^2}{\mu_y^2} + z^2 \right)^{\frac{\alpha-3}{2}} \quad (20)$$

where μ_x, μ_y are the anisotropy parameters in the x - and y -directions, respectively, α is the three dimensional spectral power law, and \tilde{C}_n^2 is the generalized refractive index structure constant with units $m^{3-\alpha}$. Although occasionally studies state this structure function model is only valid for $l_0 \ll \sqrt{x^2 + y^2 + z^2} \ll L_0$ [42], as applied to integrals for calculating second and fourth order beam statistics the inner and outer scales appear as zero and infinity, respectively. Also note that for $\alpha = 11/3$, Eq. 20 simplifies to the $2/3$'s law of Kolmogorov. It can be shown [40] that Eq. 20 corresponds to a three dimensional energy spectrum:

$$\Phi_n(\kappa_x, \kappa_y, \kappa_z) = \frac{A(\alpha) \tilde{C}_n^2 \mu_x \mu_y}{(\mu_x^2 \kappa_x^2 + \mu_y^2 \kappa_y^2 + \kappa_z^2)^{\alpha/2}} \quad (21)$$

$$A(\alpha) = \frac{\cos(\frac{\pi\alpha}{2}) \Gamma(\alpha-1)}{4\pi^2} \quad (22)$$

where Γ denotes the gamma function.

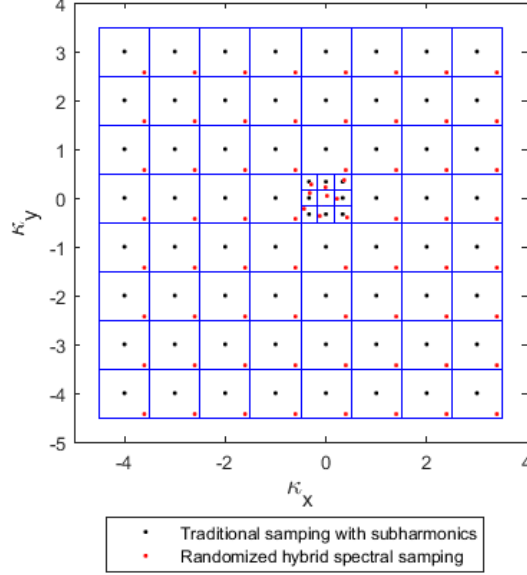


Figure 6: Visual aid showing traditional subharmonic sampling approach versus hybrid randomized spectral sampling approach in κ -space for $N_p = 1$. Black dots represent traditional sampling points (including subharmonic expansion), red dots represent one realization of the randomized sampling approach, and the blue grid lines demarcate the sampling boundaries for the randomized method.

These spectral models do not address practical matters of maximum feature sizes (outer scales) or Kolmogorov microscales (inner scales), where the internal subrange ends and dissipation is the primary form of energy transfer [46, 47]. However, these models are useful for studies of non-classical turbulence when the inertial subrange can be approximated as infinite. While great attention has so far been devoted to modeling low spatial frequency components, very little emphasis is placed on high frequency components outside of the simulated κ -space. As demonstrated in Figs. 7 and 8, this results in a *sag* of the phase screen structure relative to theory over small distances.

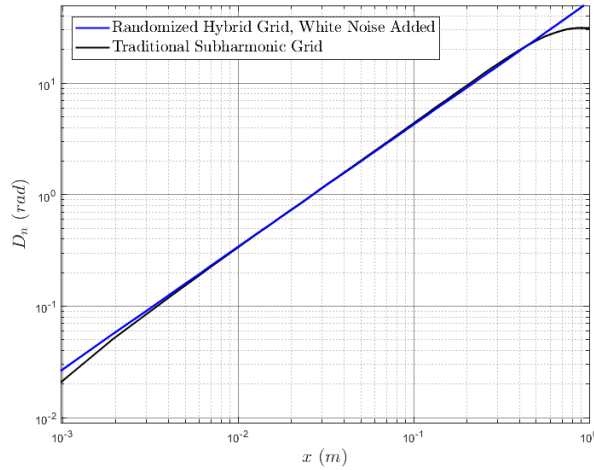


Figure 7: x -axis structure of phase screens made with the randomized, hybrid subharmonic algorithm and white noise added, as well as screens using the traditional subharmonic method. Parameters for the screens are 1024×1024 grid, $N_p = 1$, $\alpha = 3.1$, $\lambda = 1060$ nm, $\Delta z = 500$ m, and $\tilde{C}_n^2 = 10^{-14} \text{ m}^{-0.1}$.

We attempt to resolve this problem via addition of white noise to the screen, in order to simulate spectral energy not included in the κ -space sampling grid or subharmonic subgrids. Recalling the formation of the structure function in Eq.

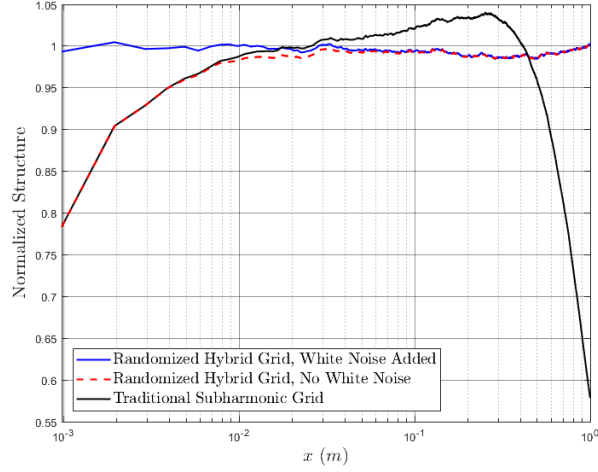


Figure 8: x -axis structure normalized by theory of phase screens made with the randomized, hybrid subharmonic algorithm both with and without white noise added, as well as screens using the traditional subharmonic method. The parameters used to create this figure are identical to those of Fig. 7.

11, we calculate the variance of the white noise to be added to the screen as per the set of area integrals:

$$\sigma_x^2 = 2\pi\Delta z\tilde{C}_n^2k^2 \iint_{K_{out}} \Phi_n(\kappa_x, \kappa_y, 0) [1 - \cos(x\kappa_x)] d\kappa_x d\kappa_y \quad (23)$$

$$\sigma_y^2 = 2\pi\Delta z\tilde{C}_n^2k^2 \iint_{K_{out}} \Phi_n(\kappa_x, \kappa_y, 0) [1 - \cos(y\kappa_y)] d\kappa_x d\kappa_y \quad (24)$$

where K_{out} represents the region spanning all of the $\kappa_z = 0$ plane, which we define explicitly via:

$$K = \left\{ (\kappa_x, \kappa_y) : \begin{aligned} &-\infty < \kappa_x < \infty, \\ &-\infty < \kappa_y < \infty \end{aligned} \right\} \quad (25)$$

$$K_{in} = \left\{ (\kappa_x, \kappa_y) : \begin{aligned} &-\Delta\kappa_x \frac{M}{2} < \kappa_x < \Delta\kappa_x \frac{M-1}{2}, \\ &-\Delta\kappa_y \frac{M}{2} < \kappa_y < \Delta\kappa_y \frac{M-1}{2} \end{aligned} \right\} \quad (26)$$

$$K_{out} = \left\{ (\kappa_x, \kappa_y) : (\kappa_x, \kappa_y) \in K \mid (\kappa_x, \kappa_y) \notin K_{in} \right\} \quad (27)$$

In practice, the variances of Eqs. 23 and 24 can be evaluated numerically as the sum of several integrals. For the data sets in this article, four integrals per parameter set were used spanning from the each corner of K_{in} to a $|\kappa_x|, |\kappa_y| = \infty$ point in an adjacent quadrant of κ -space. Finally, the variances of two white noise processes are calculated as:

$$\sigma_1^2 = \text{Minimum}(\sigma_x^2, \sigma_y^2) \quad (28)$$

$$\sigma_2^2 = |\sigma_x^2 - \sigma_y^2| \quad (29)$$

In order to *whiten* our phase screens, a $M \times M$ matrix of Gaussian white noise with variance σ_1^2 is added to the screen, and is followed by addition of a random number with variance σ_1^2 across each column (if $\sigma_x^2 > \sigma_y^2$) or row (if $\sigma_y^2 > \sigma_x^2$) of the grid. For isotropic turbulence $\sigma_x^2 = \sigma_y^2$, $\sigma_2^2 = 0$, and the second step can be negated. This method ensures the small scale structure across the x -, y -, and diagonal directions is improved relative to theory.

Figures 7 and 8 show qualitative results of using this method. As lower power law α values place a higher portion of their spectral energy at high frequencies, we have chosen to display a power law of $\alpha = 3.1$.

3.3 Results for Bounded Spectral Models

Returning to the modified atmospheric spectrum discussed in Section 22.2, we observe a marked difference in accuracy of the hybrid method vs the subharmonic method of Frehlich [14], which we refer to interchangeably as the *traditional subharmonic method*. We have chosen to compare with this specific subharmonic method, as opposed to other candidates [13, 48] due to its improved convergence with theory [14] by virtue of weighting the subharmonic amplitude variances using area integrals of spectral models of interest, as opposed to (non-randomized) spectral samplings. Results for several values of the outer scale, L_0 , are shown in Fig. 9, with full results given in Tables 1 and 2. For each case, the size of the outer scale has been set as a factor of the total simulated x -, y -basis, which was always one meter for this simulation set (i.e. $M\Delta x = 1$ for all bounded spectrum data sets). Because it is impractical to present data for all grid sizes, outer scales, and number of subharmonic constellations, we have focused on the 2048×2048 grid case.

The data in this subsection represents statistics taken from a large sampling of phase screens, along the $\frac{M}{2} + 1$ ordered row and column of each screen. Because the sampling directions are orthogonal the sample set sizes are, essentially, 10,000 trials. We find that for each case the hybrid method outperforms the traditional subharmonic method, which can be verified by close inspection of Tables 1 and 2. In general, the RMS error over the region of interest in the phase screens can be driven to 3% or below with the addition of enough subharmonics. Again comparing Tables 1 and 2, we find that the error ratio of the hybrid method with the subharmonic method can be as low as 13.3%.

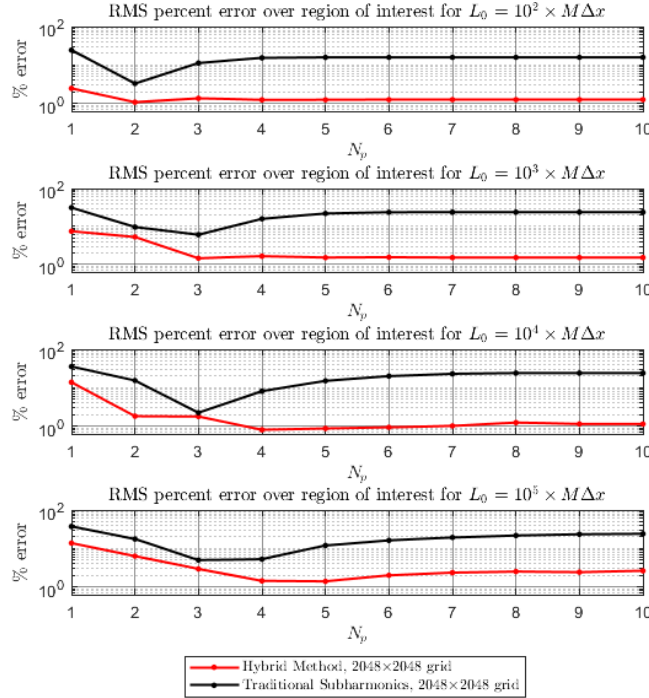


Figure 9: RMS error over region of interest computed along x - and y -directions for 5,000 phase screens using modified spectrum, with $l_0 = M\Delta x/100$.

3.4 Results for Unbounded Spectral Models

We also wish to assess the accuracy of our revised algorithm for the cases of generalized anisotropic, non-Kolmogorov turbulence spectra discussed in Section 33.2. Although in the previous Section the theoretical structure metric was computed using numeric integration, in this case simple closed-form solutions exist. By applying a change of variable to Eq. 11 and we obtain:

$$D_\theta(x, y) = 8\pi^2 k^2 A(\alpha) B(\alpha) \tilde{C}_n^2 \Delta z \left(\frac{x^2}{\mu_x^2} + \frac{y^2}{\mu_y^2} \right)^{\frac{\alpha-2}{2}} \quad (30)$$

-	Number of Subharmonic Constellations, N_p									
L_0	1	2	3	4	5	6	7	8	9	10
10^0	1.7	1.7	1.7	1.7	1.7	1.7	1.7	1.7	1.7	1.7
$10^{.5}$	2.8	3.0	3.0	3.0	3.0	3.0	3.0	3.0	3.0	3.0
10^1	2.4	2.7	2.7	2.6	2.6	2.6	2.6	2.6	2.6	2.6
$10^{1.5}$	2.8	3.4	2.9	2.7	2.7	2.7	2.7	2.7	2.7	2.7
10^2	2.5	1.1	1.4	1.2	1.3	1.3	1.3	1.3	1.3	1.3
$10^{2.5}$	2.6	1.1	1.3	1.1	1.3	1.3	1.3	1.3	1.3	1.3
10^3	7.5	5.3	1.4	1.6	1.5	1.5	1.5	1.5	1.5	1.5
$10^{3.5}$	10	1.6	1.5	1.5	1.1	1.3	1.4	1.3	1.3	1.3
10^4	14	1.8	1.8	0.8	0.9	0.9	1.0	1.2	1.2	1.1
$10^{4.5}$	7.4	7.0	1.8	1.6	1.9	1.9	1.5	1.5	1.6	1.6
10^5	14	6.4	3.0	1.4	1.4	2.0	2.4	2.5	2.4	2.6

Table 1: Hybrid method percent RMS error compared to theory over region of interest computed using 5,000 phase screens' x - and y -axes for 2048×2048 grid size, parameterized by outer scale, L_0 , as well as the number of subharmonic constellations, N_p . The L_0 's given in the first column have units of meters, and the simulated basis was a one meter by one meter area.

-	Number of Subharmonic Constellations, N_p									
L_0	1	2	3	4	5	6	7	8	9	10
10^0	2.1	2.2	2.2	2.2	2.2	2.2	2.2	2.2	2.2	2.2
$10^{0.5}$	5.9	4.8	4.8	4.8	4.8	4.8	4.8	4.8	4.8	4.8
10^1	5.4	4.5	4.9	4.8	4.8	4.8	4.8	4.8	4.8	4.8
$10^{1.5}$	14	7.6	13	14	14	14	14	14	14	14
10^2	24	3.3	11	15	16	16	16	16	16	16
$10^{2.5}$	30	7.9	8.5	17	20	20	20	20	20	20
10^3	31	9.7	6.1	16	22	24	24	24	24	24
$10^{3.5}$	35	15	2.6	8.8	17	22	23	23	23	23
10^4	36	15	2.2	8.2	15	20	23	24	24	24
$10^{4.5}$	36	16	2.7	7.6	14	19	22	24	25	25
10^5	37	18	5.0	5.3	12	16	19	22	23	24

Table 2: Traditional method percent RMS error compared to theory over region of interest in similar configuration as described in Table 1.

$B(\alpha)$ is defined in terms of a Bessel function integral identity [49]:

$$\begin{aligned}
 B(\alpha) &= \int_0^\infty (1 - J_0(\kappa_\rho)) \kappa_\rho^{(1-\alpha)} d\kappa_\rho \\
 &= \frac{\pi \cdot \sec\left(\pi \frac{\alpha-3}{2}\right)}{2^{\alpha-1} \Gamma^2\left(\frac{\alpha}{2}\right)}
 \end{aligned} \tag{31}$$

where \sec denotes the secant function. Substituting $D_\theta(j\Delta x, 0)$ and $D_\theta(0, l\Delta y)$ for the theoretical error expressions of Eqs. 13 and 14, respectively, allows us to again use Eq. 15 as our error metric.

Due to the combination of our assessment of error as a ratio relative to a theory, as well as the scale invariance [13] of this section's turbulence models, the specific \tilde{C}_n^2 and basis lengths, $M\Delta x$ and $M\Delta y$, do not affect results. The results are, however, sensitive to the α in use and number of subharmonics constellations. Figure 10 displays a comparison of the hybrid method, including whitening, versus the Frehlich subharmonic method for several α 's over 50,000 independent, 1024×1024 resolution phase screens using numbers of constellations between zero and ten. We note that data was also collected for α 's of 3.2, 3.4, 3.6, 3.7, and 3.8 up to $N_p = 10$ however that data is not plotted. Table 3 summarizes the minimum errors observed in testing for both schemes, as well as associated N_p . We have observed that our hybrid method outperforms the Frehlich subharmonic method on the 1024×1024 grid for any number of subharmonic constellations, except for $\alpha = 3.9$. Noting that our revised method falls short for the $\alpha = 3.9$ case (at least for $N_p \leq 10$), comparing the minimum \mathcal{E} observed using each method for $\alpha = 3.1$ to 3.8 we note that the average ratio of our hybrid method's \mathcal{E} to that of the Frehlich method is 7.4%.

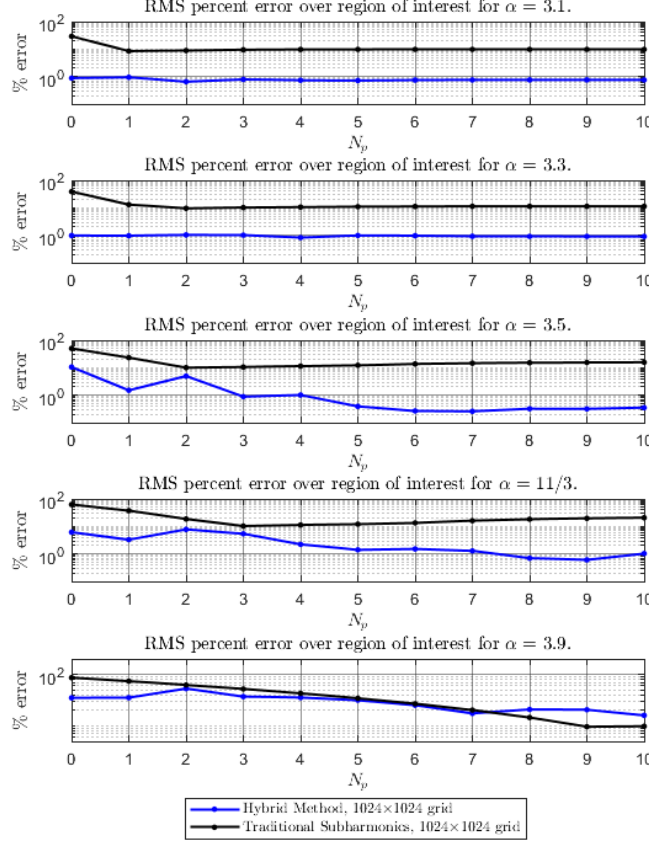


Figure 10: RMS error over region of interest computed along x - and y -directions of 50,000 phase screens for 1024×1024 grid using various spectral power laws (α 's) and number of subharmonic constellations, N_p . $\mu_x = 1$ and $\mu_y = 2$ for all data points.

α	3.1	3.2	3.3	3.4	3.5	3.6	$\frac{11}{3}$	3.7	3.8	3.9
N_p	2	3	4	3	7	10	9	5	7	10
\mathcal{E}	.65	.33	.82	.86	.26	.46	.61	.55	1.9	16
N_p	1	2	2	2	2	3	3	4	5	9
\mathcal{E}	8.5	9.7	9.6	9.5	10	10	10	10	9.7	9.6

Table 3: Minimum percent RMS error (\mathcal{E}) and associated number of subharmonic constellations (N_p) for Randomized Hybrid Method (middle two rows) versus traditional method (bottom two rows) for $N_p \leq 10$. Data was collected over 50,000 phase screens for 1024×1024 grid, $\mu_x = 1$ and $\mu_y = 2$.

We have also included results for a 2048×2048 grid case, as shown in Fig. 11. These metrics were gathered using a smaller number of total phase screens (5,000) due to the longer computation times associated with the larger grid sizes. For $\alpha \geq 11/3$ we have included results up to $N_p = 20$ in order to demonstrate that for higher α 's performance improvements appear to continue as subharmonic constellations above 10 are added. Results for select α 's are shown in Figure 11, with We should note that due to the smaller number of total phase screens assessed, the statistical trends appear noisier than the 1024×1024 grid case. Additionally, due to the overall lower error numbers for $\alpha < 3.8$ collected using the 1024×1024 grid over a greater number of sampled, we believe it is good assumption the higher resolution 2048×2048 grid results would be improved with a larger sampling phase screens under test. For the 2048×2048 grid case, the average ratio of the randomized hybrid method's \mathcal{E} to that of the traditional subharmonic method is 15.1% across all α 's under test.

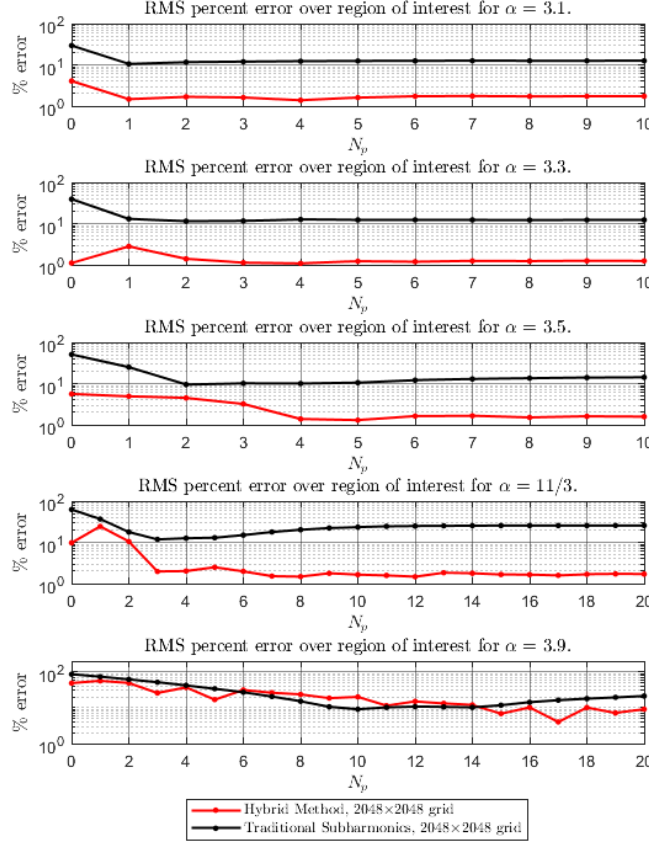


Figure 11: RMS error over region of interest computed along x - and y -directions of 5,000 phase screens for 2048×2048 grid using various α 's. A maximum of ten subharmonic constellations were used for α 's below $11/3$, and a twenty subharmonic constellation maximum was used for α 's greater than or equal to $11/3$. $\mu_x = 1$ and $\mu_y = 2$ for all data points.

α	3.1	3.2	3.3	3.4	3.5	3.6	$\frac{11}{3}$	3.7	3.8	3.9
N_p	4	3	4	4	5	7	12	8	17	17
\mathcal{E}	1.4	1.3	1.1	1.5	1.3	.95	1.5	1.2	1.3	4.0
N_p	1	2	2	2	2	3	3	4	5	10
\mathcal{E}	11	11	11	8.2	9.5	13	12	11	13	9.1

Table 4: Minimum percent RMS error (\mathcal{E}) and associated number of subharmonic constellations (N_p) for Randomized Hybrid Method (middle two rows) versus traditional method (bottom two rows). Data was collected over 5,000 phase screens for 2048×2048 grid, $\mu_x = 1$ and $\mu_y = 2$.

4 Conclusion and Discussion

In this work we have demonstrated a straightforward method to correct low spatial frequency and periodicity issues associated with FFT-based phase screen methods. We have further demonstrated that low and high spatial frequency contributions can be further improved by combining our core technique with supplemental methods. In previous work [38] we have estimated that the addition of every subharmonic constellations adds approximately the same computation time of generating the purely FFT-based phase screen. As in many cases the core algorithm sans subharmonics outperforms other methods utilizing multiple subharmonics, significant computation time associated with creating the screens may be conserved while garnering improved structure accuracy. In cases where accuracy is paramount, our hybrid method is able to produce very low error percentages across the region of interest.

Aside from the stated application of simulation of atmospheric optical turbulence, utilizing randomized spectral sampling in concert with the FFT may have additional applications. When modelling processes containing divergences or nulls in their spectral representations we believe a modification of our algorithm giving in Section 22.1 should be

considered. Simulations of processes approximated by fractional differencing [50], such as radio frequency oscillator phase noise [51], are a potential candidate. The $1/f^\alpha$ spectral model (with f the time frequency) of the stochastic process is similar to our own. Additionally, straightforward applications would be to apply the techniques outlined in this study to simulations of partially coherent sources [52, 53], simulations using three-dimensionally correlated phase screens [54, 55], and simulations of optical propagation in underwater turbulence, which has its own unique spectral representations [56, 57, 58]. The heightened low spatial frequency accuracy our techniques will have a direct impact on beam wander statistics, which have been shown as an important factor in free space optical (FSO) communications [59, 60, 61]. Additionally, temporal statistics are often at the center of studies regarding FSO performance metrics [62, 63, 64, 61], which has lead to research on long phase screens to simulate aperiodic turbulence moving at the wind speed [59, 65, 66]. We note that through a combination of circularly shifting the C matrix of Eq. 6 and applying multiplying the exponential term in Eq. 7 by a factor, we have successfully demonstrated the creation of aperiodic moving phase screens derived from the original components of θ_R , but not requiring the use of additional FFT's after the first complex screen realization (see Supplemental Information). Extending this capability to include subharmonic constellations is not challenging. This feature can be directly applied to simulations of time-domain turbulence affects, or combined with other techniques [66, 67] to improve statistics.

5 Supplemental Material

5.1 Aliasing Issues of FFT-based Phase Screens

In Section 22.1 it was mentioned that care must be taken in defining the refractive index spectral power function, Φ_n , and by extension the random function, \tilde{c} . More explicitly, Φ_n used in Eq. 4 should be given by the replacement:

$$\Phi_n \left(\left(\kappa_x + \Delta\kappa_x \frac{M+1}{2} \% M\Delta\kappa_x \right) - \Delta\kappa_x \frac{M+1}{2}, \right. \\ \left. \left(\kappa_y + \Delta\kappa_y \frac{M+1}{2} \% M\Delta\kappa_y \right) - \Delta\kappa_y \frac{M+1}{2} \right) \quad (32)$$

where $\%$ in Eq. 32 represents the modulo operator. Additionally, this substitution explains the grid boundaries of Figs. 1 and 6 relative to Eqs. 3 and 4.

5.2 Replacement of Inverse FFT in Randomized Algorithm

As alluded to in in Section 22.1, the M^2 in Eq. 6 may be dropped and the FFT used to achieve the same complex phase screen via:

$$C(j, l) = M^2 \cdot \mathcal{F}_2^{-1} \left[\tilde{C}(n, m) \right] \\ = \mathcal{F}_2^* \left[\tilde{C}^*(n, m) \right] \quad (33)$$

where $\mathcal{F}_2[\cdot]$ denotes the 2-dimensional FFT operator, and $*$ the complex conjugate. Complex conjugation can also be skipped by effectively flipping the 2^{nd} to M^{th} elements of each row and column of \tilde{C} . This can be attained using the modulo operator by virtue of:

$$\mathcal{F}_2 \left[\tilde{C}((M - n + 1 \% M) + 1, (M - n + 1 \% M) + 1) \right] \quad (34)$$

However, in practice it is only important the statistics of the screens in question are reproduced. This can be achieved simply using:

$$C(j, l) = \mathcal{F}_2[\tilde{C}(n, m)] \quad (35)$$

$$\theta_R(j, l) = \exp[-i(j\Delta x\delta\kappa_x + l\Delta y\delta\kappa_y)] \cdot C(j, l) \quad (36)$$

where we note we have changed the sign in the exponent in Eq. 36 to be the opposite of that in Eq. 7.

5.3 Moving Phase Screens

As discussed in Section 4 it is possible to create moving screens using our modified algorithm from Section 22.1. Should one wish to move the screens by an integer number of pixels each time step, this can be implemented by circularly

shifting [24] the matrix defined by $C(j, l)$ each iteration of a loop, and applying a proper multiplicative term to again utilize the shift theorem [24, 25]. Let $C'(j, l, t)$ define the shifted C -defined matrix for each step, t . When using the inverse FFT to create phase screens, the desired shifted screen, $\theta'_R(j, l, t)$, is given by:

$$\theta'_R(j, l, t) = \mathcal{P}(j, l, t) \cdot C'(j, l, t) \quad (37)$$

where $\mathcal{P}(j, l, t)$ is given by:

$$\begin{aligned} \mathcal{P}(j, l, t) = & \exp[-i(\delta\kappa_x v_x t + \delta\kappa_y v_y t)] \\ & \cdot \exp[i(j\Delta x \delta\kappa_x + l\Delta y \delta\kappa_y)] \end{aligned} \quad (38)$$

where v_x and v_y is the velocity of simulated motion in units of meters per iteration. We note that when using the FFT convention, as per Section 55.2, the signs in both exponents in Eq. 38 must be inverted. To avoid precision issues for large t , we recommend computing $\mathcal{P}(j, l, t)$ iteratively as per:

$$\begin{aligned} \mathcal{P}(j, l, t) &= \exp[i(j\Delta x \delta\kappa_x + l\Delta y \delta\kappa_y)], & t = 0 \\ &= \exp[-i(\delta\kappa_x v_x + \delta\kappa_y v_y)] \cdot \mathcal{P}(j, l, t-1), & t \geq 1 \end{aligned} \quad (39)$$

If movement by a non-integer number of pixels is desired, one can interpolate $C'(j, l, t-1)$ from step to step, or use:

$$\begin{aligned} \tilde{C}'(n, m, t) &= \tilde{C}(n, m), & t = 0 \\ &= \exp[i(n\Delta\kappa_x v_x + m\Delta\kappa_y v_y)] \tilde{C}'(n, m, t-1), & t \geq 1 \end{aligned} \quad (40)$$

Please see Section 22.1 for our definition of $\tilde{C}(n, m)$. The $C'(j, l, t)$ for use in Eq. 37 is then given by:

$$\begin{aligned} C'(n, m, t) &= M^2 \cdot \mathcal{F}^{-1} [\tilde{C}'(n, m, t)] \\ &= \mathcal{F}^* [\tilde{C}'^*(n, m, t)] \end{aligned} \quad (41)$$

Note that previous statements regarding interchange of inverse FFT with the FFT without complex conjugation for statistical equivalence also apply to Eq. 41. Should one desire to drop the complex conjugation in the FFT based method of Eq. 41 the sign of exponents in our definition of $\mathcal{P}(j, l, t)$ in Eq. 38 and 39 must be inverted appropriately, along with the exponent of Eq. 40.

6 Funding Information

This work was supported by the Office of Naval Research (ONR) Atmospheric Propagation Studies for High Energy Lasers (APSHEL) program under grant N000141812008.

References

- [1] J. A. Fleck, J. R. Morris, and M. D. Feit. Time-dependent propagation of high energy laser beams through the atmosphere. *Applied Physics*, 10(2):129–160, Jun 1976.
- [2] J. A. Fleck, J. R. Morris, and M. D. Feit. Time-dependent propagation of high-energy laser beams through the atmosphere: II. *Applied Physics*, 14(1):99–115, Sep 1977.
- [3] Phillip Sprangle, Joseph R. Peñano, Antonio Ting, and Bahman Hafizi. Incoherent combining of high-power fiber lasers for long-range directed energy applications. Technical Report NRL/MR/6790–06-8963, Naval Research Laboratory, Washington, DC, June 2006.
- [4] Phillip Sprangle, Joseph R. Peñano, and Bahman Hafizi. Beam combining and atmospheric propagation of high power lasers. Technical Report NRL/MR/6790–11-9371, Naval Research Laboratory, Washington, DC, November 2011.
- [5] J.P. Palastro, J. Peñano, W. Nelson, G. DiComo, M. Helle, L. A. Johnson, and B. Hafizi. Reciprocity breaking during nonlinear propagation of adapted beams through random media. *Opt. Express*, 24(17):18817–18827, Aug 2016.
- [6] Jonathan Gustafsson, Benjamin F. Akers, Jonah A. Reeger, and Sivaguru S. Sritharan. Atmospheric propagation of high energy lasers: Thermal blooming simulation. *Engineering Mathematics Letters (to be published)*, 2019.
- [7] V P Kandidov, O G Kosareva, M P Tamarov, A Brodeur, and S L Chin. Nucleation and random movement of filaments in the propagation of high-power laser radiation in a turbulent atmosphere. *Quantum Electronics*, 29(10):911–915, oct 1999.

- [8] S.L. Chin, A. Talebpour, J. Yang, S. Petit, V.P. Kandidov, O.G. Kosareva, and M.P. Tamarov. Filamentation of femtosecond laser pulses in turbulent air. *Applied Physics B*, 74(1):67–76, Jan 2002.
- [9] J. R. Peñano, P. Sprangle, B. Hafizi, A. Ting, D. F. Gordon, and C. A. Kapetanakis. Propagation of ultra-short, intense laser pulses in air. *Physics of Plasmas*, 11(5):2865–2874, 2004.
- [10] A. Couairon and A. Mysyrowicz. Femtosecond filamentation in transparent media. *Physics Reports*, 441(2):47 – 189, 2007.
- [11] A. Houard, M. Franco, B. Prade, A. Durécu, L. Lombard, P. Bourdon, O. Vasseur, B. Fleury, C. Robert, V. Michau, A. Couairon, and A. Mysyrowicz. Femtosecond filamentation in turbulent air. *Phys. Rev. A*, 78:033804, Sep 2008.
- [12] J. Peñano, B. Hafizi, A. Ting, and M. Helle. Theoretical and numerical investigation of filament onset distance in atmospheric turbulence. *J. Opt. Soc. Am. B*, 31(5):963–971, May 2014.
- [13] R.G. Lane, A. Glindemann, and J.C. Dainty. Simulation of a kolmogorov phase screen. *Waves in Random Media*, 2(3):209–224, 1992.
- [14] Rod Frehlich. Simulation of laser propagation in a turbulent atmosphere. *Appl. Opt.*, 39(3):393–397, Jan 2000.
- [15] Nicolas A. Roddier. Atmospheric wavefront simulation using zernike polynomials. *Optical Engineering*, 29:29 – 29 – 7, 1990.
- [16] Mikhail Charnotskii. Sparse spectrum model for a turbulent phase. *J. Opt. Soc. Am. A*, 30(3):479–488, Mar 2013.
- [17] William P. Burckel and Ryan N. Gray. Turbulence phase screens based on polar-logarithmic spectral sampling. *Appl. Opt.*, 52(19):4672–4680, Jul 2013.
- [18] Xifeng Xiao and David Voelz. Wave optics simulation approach for partial spatially coherent beams. *Opt. Express*, 14(16):6986–6992, Aug 2006.
- [19] Jason D. Schmidt. *Numerical Simulation of Optical Wave Propagation with Examples in MATLAB*. SPIE, Bellingham, Wash, 2010.
- [20] W. Nelson, J. P. Palastro, C. C. Davis, and P. Sprangle. Propagation of bessel and airy beams through atmospheric turbulence. *J. Opt. Soc. Am. A*, 31(3):603–609, Mar 2014.
- [21] W. Nelson, J. P. Palastro, C. Wu, and C. C. Davis. Enhanced backscatter of optical beams reflected in turbulent air. *J. Opt. Soc. Am. A*, 32(7):1371–1378, Jul 2015.
- [22] Xifeng Xiao, David G. Voelz, Italo Toselli, and Olga Korotkova. Gaussian beam propagation in anisotropic turbulence along horizontal links: theory, simulation, and laboratory implementation. *Appl. Opt.*, 55(15):4079–4084, May 2016.
- [23] David G. Voelz, Erandi Wijerathna, Andreas Muschinski, and Xifeng Xiao. Computer simulations of optical turbulence in the weak- and strong-scattering regime: angle-of-arrival fluctuations obtained from ray optics and wave optics. *Optical Engineering*, 57(10):1 – 9 – 9, 2018.
- [24] Joseph W. Goodman. Analysis of two-dimensional signals and systems. In *Introduction to Fourier Optics*, chapter 2, pages 5–42. W.H. Freedman and Company, New York, 4 edition, 2017.
- [25] Sanjit Kumar Mitra. *Digital signal processing: a computer-based approach*, pages 140–143, 584–593. McGraw-Hill/Irwin, Boston, 2 edition, 2001.
- [26] Valerian I. Tatarskii. *Wave Propagation in a Turbulence Medium*, pages 8–14, 27–39. Dover, Mineola, New York, 1969.
- [27] R. J. Hill. Models of the scalar spectrum for turbulent advection. *Journal of Fluid Mechanics*, 88(3):541–562, 1978.
- [28] L.C. Andrews. An analytical model for the refractive index power spectrum and its application to optical scintillations in the atmosphere. *Journal of Modern Optics*, 39(9):1849–1853, 1992.
- [29] Larry C. Andrews and Ronald L. Phillips. Optical turbulence in the atmosphere. In *Laser Beam Propagation through Random Media*, chapter 3, pages 57–82. SPIE, Bellingham, Wash, 2005.
- [30] F. H. Champagne, C. A. Friehe, J. C. LaRue, and J. C. Wynagaard. Flux measurements, flux estimation techniques, and fine-scale turbulence measurements in the unstable surface layer over land. *Journal of the Atmospheric Sciences*, 34(3):515–530, 1977.
- [31] R. M. Williams and C. A. Paulson. Microscale temperature and velocity spectra in the atmospheric boundary layer. *Journal of Fluid Mechanics*, 83(3):547–567, 1977.
- [32] L.C. Andrews, S. Vester, and C.E. Richardson. Analytic expressions for the wave structure function based on a bump spectral model for refractive index fluctuations. *Journal of Modern Optics*, 40(5):931–938, 1993.

- [33] Justin D. Mansell, Robert Praus, and Steve Coy. Determining wave-optics mesh parameters for complex optical systems. *Proc. SPIE 6675, Optical Modeling and Performance Predictions*, III:66750H, Sep 2007.
- [34] Steve Coy. Choosing mesh spacings and mesh dimensions for wave optics simulation. *Proc. SPIE 5894, Advanced Wavefront Control: Methods, Devices, and Applications*, III:589405, Aug 2005.
- [35] Stanley M. Flatté, Guang-Yu Wang, and Jan Martin. Irradiance variance of optical waves through atmospheric turbulence by numerical simulation and comparison with experiment. *J. Opt. Soc. Am. A*, 10(11):2363–2370, Nov 1993.
- [36] K. D. Ridley and E. Jakeman. Incomplete phase conjugation through a random phase screen. ii. numerical simulations. *J. Opt. Soc. Am. A*, 13(12):2393–2402, Dec 1996.
- [37] Chensheng Wu, John R. Rzasa, Jonathan Ko, Daniel A. Paulson, Joseph Coffaro, Jonathan Spsychalsky, Robert F. Crabbs, and Christopher C. Davis. Multi-aperture laser transmissometer system for long-path aerosol extinction rate measurement. *Appl. Opt.*, 57(3):551–559, Jan 2018.
- [38] Daniel A. Paulson, Chensheng Wu, and Christopher C. Davis. A detailed comparison of non-kolmogorov and anisotropic optical turbulence theories using wave optics simulations. *Proc. SPIE 10770, Laser Communication and Propagation through the Atmosphere and Oceans*, VII:107700K, 2018.
- [39] A I Kon. Qualitative theory of amplitude and phase fluctuations in a medium with anisotropic turbulent irregularities. *Waves in Random Media*, 4(3):297–306, 1994.
- [40] Italo Toselli, Larry C. Andrews, Ronald L. Phillips, and Valter Ferrero. Free-space optical system performance for laser beam propagation through non-kolmogorov turbulence. *Optical Engineering*, 47(2):1 – 9 – 9, 2008.
- [41] Italo Toselli, Brij Agrawal, and Sergio Restaino. Light propagation through anisotropic turbulence. *J. Opt. Soc. Am. A*, 28(3):483–488, Mar 2011.
- [42] L. C. Andrews, R. L. Phillips, R. Crabbs, and T. Leclerc. Deep turbulence propagation of a gaussian-beam wave in anisotropic non-kolmogorov turbulence. *Proc. SPIE 8874, Laser Communication and Propagation through the Atmosphere and Oceans*, II:887402, 2013.
- [43] L. C. Andrews, R. L. Phillips, and R. Crabbs. Propagation of a gaussian-beam wave in general anisotropic turbulence. *Proc. SPIE 9224, Laser Communication and Propagation through the Atmosphere and Oceans*, III:922402, 2014.
- [44] Fei Wang and Olga Korotkova. Random optical beam propagation in anisotropic turbulence along horizontal links. *Opt. Express*, 24(21):24422–24434, Oct 2016.
- [45] Melissa Beason, Christopher Smith, Joseph Coffaro, Sara Belichki, Jonathon Spsychalsky, Franklin Titus, Robert Crabbs, Larry Andrews, and Ronald Phillips. Near ground measure and theoretical model of plane wave covariance of intensity in anisotropic turbulence. *Opt. Lett.*, 43(11):2607–2610, Jun 2018.
- [46] S. Mostafa Ghiaasiaan. Fundamental of turbulence and external turbulent flow. In *Convective Heat and Mass Transfer*, chapter 6, pages 177 – 207. Cambridge University Press, New York, 2011.
- [47] R. L. Fante. Electromagnetic beam propagation in turbulent media. *Proceedings of the IEEE*, 63(12):1669–1692, Dec 1975.
- [48] Erik M. Johansson and Donald T. Gavel. Simulation of stellar speckle imaging. *Proceedings SPIE 2200, Amplitude and Intensity Spatial Interferometry*, II:372–383, 1994.
- [49] *NIST Digital Library of Mathematical Functions*. <http://dlmf.nist.gov/>, Release 1.0.22 of 2019-03-15. F. W. J. Olver, A. B. Olde Daalhuis, D. W. Lozier, B. I. Schneider, R. F. Boisvert, C. W. Clark, B. R. Miller and B. V. Saunders, eds.
- [50] J.R.M. HOSKING. Fractional differencing. *Biometrika*, 68(1):165–176, 04 1981.
- [51] D. B. Leeson. Oscillator phase noise: A 50-year review. *IEEE Transactions on Ultrasonics, Ferroelectrics, and Frequency Control*, 63(8):1208–1225, Aug 2016.
- [52] A. Schell. A technique for the determination of the radiation pattern of a partially coherent aperture. *IEEE Transactions on Antennas and Propagation*, 15(1):187–188, January 1967.
- [53] Aristide Dogariu and Stefan Amarande. Propagation of partially coherent beams: turbulence-induced degradation. *Optics Letters*, 28(1):10–12, Jan 2003.
- [54] Itay Naeh and Abraham Katzir. Perfectly correlated phase screen realization using sparse spectrum harmonic augmentation. *Appl. Opt.*, 53(27):6168–6174, Sep 2014.
- [55] Parisa Fatheddin and Jonathan Gustafsson. Generation of a sequence of correlated phase screens. *Optics Communications*, 391:100 – 105, 2017.

- [56] L. Goodman. Acoustic scattering from ocean microstructure. *Journal of Geophysical Research: Oceans*, 95(C7):11557–11573, 1990.
- [57] O. Korotkova, N. Farwell, and E. Shchepakina. Light scintillation in oceanic turbulence. *Waves in Random and Complex Media*, 22(2):260–266, 2012.
- [58] Weilin Hou, Ewa Jarosz, Sarah Woods, Wesley Goode, and Alan Weidemann. Impacts of underwater turbulence on acoustical and optical signals and their linkage. *Opt. Express*, 21(4):4367–4375, Feb 2013.
- [59] Federico Dios, Juan Antonio Rubio, Alejandro Rodríguez, and Adolfo Comerón. Scintillation and beam-wander analysis in an optical ground station-satellite uplink. *Applied Optics*, 43(19):3866–3873, Jul 2004.
- [60] Larry C. Andrews, Ronald L. Phillips, Richard J. Sasiela, and Ronald R. Parenti. Strehl ratio and scintillation theory for uplink gaussian-beam waves: beam wander effects. *Optical Engineering*, 45(7):076001, 2006.
- [61] Santasri Basu and David Voelz. Tracking in a ground-to-satellite optical link: effects due to lead-ahead and aperture mismatch, including temporal tracking response. *J. Opt. Soc. Am. A*, 25(7):1594–1608, Jul 2008.
- [62] H. T. Yura and W. G. McKinley. Optical scintillation statistics for ir ground-to-space laser communication systems. *Appl. Opt.*, 22(21):3353–3358, Nov 1983.
- [63] Xiaoming Zhu and Joseph M. Kahn. Free-space optical communication through atmospheric turbulence channels. *IEEE Transactions on Communications*, 50(8):1293–1300, Aug 2002.
- [64] Xiaoming Zhu, J. M. Kahn, and Jin Wang. Mitigation of turbulence-induced scintillation noise in free-space optical links using temporal-domain detection techniques. *IEEE Photonics Technology Letters*, 15(4):623–625, April 2003.
- [65] François Assémat, Richard W. Wilson, and Eric Gendron. Method for simulating infinitely long and non stationary phase screens with optimized memory storage. *Optics Express*, 14(3):988–999, Feb 2006.
- [66] A. M. Vorontsov, P. V. Paramonov, M. T. Valley, and M. A. Vorontsov. Generation of infinitely long phase screens for modeling of optical wave propagation in atmospheric turbulence. *Waves in Random and Complex Media*, 18(1):91–108, 2008.
- [67] Rachel A. Johnston and Richard G. Lane. Modeling scintillation from an aperiodic kolmogorov phase screen. *Appl. Opt.*, 39(26):4761–4769, Sep 2000.